



Low Metallicities and Old Ages for Three Ultra-diffuse Galaxies in the Coma Cluster

Meng Gu¹, Charlie Conroy¹, David Law², Pieter van Dokkum³, Renbin Yan⁴, David Wake⁵, Kevin Bundy⁶, Allison Merritt³, Roberto Abraham⁷, Jielai Zhang^{7,8,9}, Matthew Bershady¹⁰, Dmitry Bizyaev^{11,12}, Jonathan Brinkmann¹¹, Niv Drory¹³, Kathleen Grabowski¹¹, Karen Masters¹⁴, Kaike Pan¹¹, John Parejko¹⁵, Anne-Marie Weijmans¹⁶, and Kai Zhang¹⁷

¹ Department of Astronomy, Harvard University, Cambridge, MA 02138, USA

² Space Telescope Science Institute, 3700 San Martin Drive, Baltimore, MD 21218, USA

³ Astronomy Department, Yale University, New Haven, CT 06511, USA

⁴ Department of Physics and Astronomy, University of Kentucky, 505 Rose Street, Lexington, KY 40506-0057, USA

⁵ Department of Physical Sciences, The Open University, Milton Keynes, MK7 6AA, UK

⁶ Department of Astronomy and Astrophysics, University of California, Santa Cruz, CA 95064, USA

⁷ Department of Astronomy and Astrophysics, University of Toronto, 50 St. George Street, Toronto, ON M5S 3H4, Canada

⁸ Canadian Institute for Theoretical Astrophysics, University of Toronto, 60 St. George Street, 14th floor, Toronto, ON M5S 3H8, Canada

⁹ Dunlap Institute for Astronomy and Astrophysics, University of Toronto, 50 St. George Street, Toronto, ON M5S 3H4, Canada

¹⁰ Department of Astronomy, University of Wisconsin-Madison, 475N. Charter Street, Madison WI 53703, USA

¹¹ Apache Point Observatory, P.O. Box 59, Sunspot, NM 88349, USA

¹² Sternberg Astronomical Institute, Moscow State University, Moscow, Russia

¹³ McDonald Observatory, The University of Texas at Austin, 1 University Station, Austin, TX 78712, USA

¹⁴ Institute of Cosmology & Gravitation, University of Portsmouth, Dennis Sciama Building, Portsmouth, PO1 3FX, UK

¹⁵ Department of Astronomy, University of Washington, Box 351580, Seattle, WA 98195, USA

¹⁶ School of Physics and Astronomy, University of St. Andrews, North Haugh, St. Andrews KY16 9SS, UK

¹⁷ Lawrence Berkeley National Laboratory, 1 Cyclotron Road, Berkeley, CA 94720, USA

Received 2017 September 19; revised 2018 March 29; accepted 2018 March 31; published 2018 May 21

Abstract

A large population of ultra-diffuse galaxies (UDGs) was recently discovered in the Coma cluster. Here we present optical spectra of three such UDGs, DF 7, DF 44, and DF 17, which have central surface brightnesses of $\mu_g \approx 24.4\text{--}25.1$ mag arcsec⁻². The spectra were acquired as part of an ancillary program within the SDSS-IV MaNGA Survey. We stacked 19 fibers in the central regions from larger integral field units (IFUs) per source. With over 13.5 hr of on-source integration, we achieved a mean signal-to-noise ratio in the optical of 9.5 \AA^{-1} , 7.9 \AA^{-1} , and 5.0 \AA^{-1} , respectively, for DF 7, DF 44, and DF 17. Stellar population models applied to these spectra enable measurements of recession velocities, ages, and metallicities. The recession velocities of DF 7, DF 44, and DF 17 are 6599^{+40}_{-25} km s⁻¹, 6402^{+41}_{-39} km s⁻¹, and 8315^{+43}_{-43} km s⁻¹, spectroscopically confirming that all of them reside in the Coma cluster. The stellar populations of these three galaxies are old and metal-poor, with ages of $7.9^{+3.6}_{-2.5}$ Gyr, $8.9^{+4.3}_{-3.3}$ Gyr, and $9.1^{+3.9}_{-5.5}$ Gyr, and iron abundances of [Fe/H] $-1.0^{+0.3}_{-0.4}$, $-1.3^{+0.4}_{-0.4}$, and $-0.8^{+0.5}_{-0.5}$, respectively. Their stellar masses are $(3\text{--}6) \times 10^8 M_\odot$. The UDGs in our sample are as old or older than galaxies at similar stellar mass or velocity dispersion (only DF 44 has an independently measured dispersion). They all follow the well-established stellar mass–stellar metallicity relation, while DF 44 lies below the velocity dispersion–metallicity relation. These results, combined with the fact that UDGs are unusually large for their stellar masses, suggest that stellar mass plays a more important role in setting stellar population properties for these galaxies than either size or surface brightness.

Key words: galaxies: clusters: individual (Coma) – galaxies: evolution – galaxies: stellar content

1. Introduction

Spatially extended low surface brightness objects have been found in galaxy cluster environments for decades (Sandage & Binggeli 1984; Impey et al. 1988; Bothun et al. 1991; Dalcanton et al. 1997; Caldwell 2006). Progress in identifying and characterizing such objects has been accelerated by specially designed instruments and improved data reduction methods in recent years. For example, van Dokkum et al. (2015a) recently discovered a numerous population of low surface brightness ($\mu_g > 24$ mag arcsec²) galaxies with surprisingly large effective radii ($R_e > 1.5$ kpc) in the Coma cluster using the Dragonfly Telephoto Array (Abraham & van Dokkum 2014). van Dokkum et al. (2015a) referred to these objects as ultra-diffuse galaxies (UDGs).¹⁸

Many UDGs are found to have exponential-like surface brightness profiles, and axis ratios similar to dwarf spheroidal galaxies (e.g., Koda et al. 2015; van Dokkum et al. 2015a). Most UDGs in cluster environments appear to have colors that are consistent with the low-mass end of the red-sequence, indicating that they are indeed cluster members. As their name implies, their sizes are much larger compared to dwarf elliptical galaxies. Following van Dokkum et al. (2015a), more UDGs have been found in the Coma cluster. For instance, Koda et al. (2015) found more than 800 UDGs in the Coma cluster based on imaging from the Suprime-Cam on the Subaru telescope. More than 300 of these UDGs have $R_e > 1.5$ kpc (also see Yagi et al. 2016). UDGs have also been found in other nearby galaxy clusters (e.g., Mihos et al. 2015; Muñoz et al. 2015; Martínez-Delgado et al. 2016; van der Burg et al. 2016; Román & Trujillo 2017), group environments (e.g., Merritt et al. 2016), and the field (e.g., Bellazzini et al. 2017;

¹⁸ Note that the term UDG is not universally used to describe all spatially extended and low surface brightness objects.

Leisman et al. 2017). Owing to their diffuse nature, only a few UDGs have a measured spectroscopic redshift (e.g., van Dokkum et al. 2015a; Kadowaki et al. 2017).

Furthermore, some UDGs show evidence for being associated with large numbers of globular clusters (GCs; Beasley & Trujillo 2016; Beasley et al. 2016; Peng & Lim 2016; van Dokkum et al. 2016, 2017). For example, DF 17 ($M_g = -15.2$) in the Coma cluster has ≈ 30 GCs (Peng & Lim 2016), and DF 44 ($M_g = -15.7$) is associated with ≈ 70 GCs (van Dokkum et al. 2016, 2017). In addition, DF 44 was revealed to have a surprisingly high velocity dispersion for its stellar mass ($\sigma = 47_{-6}^{+8} \text{ km s}^{-1}$, van Dokkum et al. 2016). Both the high velocity dispersion and the rich GC population suggest that at least some UDGs live in relatively massive dark matter halos (e.g., $M_{\text{tot,DF 44}} \sim 10^{12} M_{\odot}$, van Dokkum et al. 2016).

There is not yet a clear picture for the formation of UDGs. One plausible formation scenario is that UDGs such as DF 44 are failed Milky Way–like galaxies that have truncated star formation very early on (e.g., van Dokkum et al. 2015b, 2016, 2017), due to strong feedback or environment-related processes. Under this scenario, UDGs should be outliers of the stellar mass–halo mass relation and have more massive dark matter halos for their stellar masses. This is supported by the high stellar velocity dispersion and the rich GC systems associated with them. Other scenarios include structural transformations via tidal interaction in the cluster environment (e.g., Collins et al. 2013; Merritt et al. 2016), or formation within dark matter halos with unusually high angular momenta (Amorisco & Loeb 2016).

While the formation of UDGs is still a puzzle, stellar population information should provide useful insights. For example, low-mass galaxies reside on a tight stellar mass–stellar metallicity relation (e.g., Kirby et al. 2013), and this relation seems to be continuous to high masses (e.g., Gallazzi et al. 2005; Kirby et al. 2013; Conroy et al. 2014). Previous work suggests that this apparently tight relation is linked to multiple effects, such as metal loss due to supernova ejecta, star formation efficiency and gas inflows (e.g., Ma et al. 2016; Lu et al. 2017). Interestingly, the special properties of UDGs, such as their diffuse structures and relatively massive dark matter halos, may also be related to the above processes. The low stellar surface density of UDGs may imply low star formation efficiency. The massive dark matter halos may imply that it is harder for UDGs to lose gas and metals due to the deep gravitational potential, but at the same time the metals in the interstellar medium may be more easily diluted. Whether UDGs follow the same stellar mass–metallicity relation as low-mass galaxies can provide us with more clues on how the above processes jointly act.

In this paper, we present the first stellar population analysis through full spectral modeling for three UDGs, DF 7, DF 44, and DF 17, in the Coma cluster based on data obtained as part of an ancillary program within the SDSS-IV/MaNGA program. The Coma cluster has a median redshift of $cz = 7090 \text{ km s}^{-1}$ (Geller et al. 1999) and a velocity dispersion $\sim 1000 \text{ km s}^{-1}$ (e.g., Colless & Dunn 1996; Mobasher et al. 2001; Rines et al. 2013; Sohn et al. 2016). All three of the UDGs have large sizes for their stellar mass ($R_{\text{eff,DF 7}} = 4.3_{-0.8}^{+1.4} \text{ kpc}$, $R_{\text{eff,DF 44}} = 4.6_{-0.8}^{+1.5} \text{ kpc}$, and $R_{\text{eff,DF 17}} = 4.4_{-0.9}^{+1.5} \text{ kpc}$; van Dokkum et al. 2015a), indicating that they are typical examples in the UDG population. We provide the first measurement of a recession velocity of DF 17 and confirmation measurements of the

recession velocities of DF 7 and DF 44. We also present the first measurement of their age and metallicity. The distance of the Coma Cluster is assumed to be 100 Mpc, which was adopted from Liu & Graham (2001). This corresponds to a distance modulus of 34.99 mag and a scale of $0.474 \text{ kpc arcsec}^{-1}$. The Galactic extinction for the Coma Cluster is $A_{\text{SDSS-g}} = 0.030 \text{ mag}$ and $A_{\text{SDSS-r}} = 0.021 \text{ mag}$ (Schlafly & Finkbeiner 2011), which is applied to the photometry in this paper. All magnitudes given in this paper are in the AB system.

2. Data

2.1. Project Overview

We make use of data obtained by the MaNGA Survey (Mapping Nearby Galaxies at Apache Point Observatory, Bundy et al. 2015; Drory et al. 2015; Yan et al. 2016a). MaNGA is a large, optical integral field spectroscopy survey with 17 deployable integral field units (IFUs; ranging from $12''$ to $32''$ in diameter), and one of the fourth-generation Sloan Digital Sky Survey (SDSS-IV) programs (Blanton et al. 2017). The primary goal of MaNGA is to obtain an integral field spectroscopy of $\sim 10,000$ nearby galaxies.

Our data comes from one of MaNGA’s ancillary programs, the Deep Coma program.¹⁹ The goal of the Deep Coma program is to study the stellar populations of various targets in the Coma Cluster and its surrounding area through long integration spectroscopy. Our targets include two brightest cluster galaxies (BCG), several additional massive elliptical galaxies, dwarf galaxies, intracluster light regions, and three UDGs: DF 44, DF 17, and DF 7.

2.2. Observations

MaNGA makes use of IFU fiber bundles to feed two dual-beam Baryonic Oscillation Spectroscopic Survey (BOSS) spectrographs (Smee et al. 2013; Drory et al. 2015) that are on the SDSS 2.5 m telescope (Gunn et al. 2006). The spectrographs have 1423 fibers in total that are bundled into different size IFUs. The diameter of each fiber is $1''98$ on the sky. The wavelength coverage of the spectrographs is 3622–10354 Å with a $\sim 400 \text{ Å}$ overlap from $\sim 5900 \text{ Å}$ to $\sim 6300 \text{ Å}$. The spectral resolution is 1560–2650.

The Deep Coma project consists of six plates designed to observe selected targets in the Coma cluster. The centers of all plates are at R.A. = $12^{\text{h}}58^{\text{m}}35^{\text{s}}.58$, decl. = $27^{\text{d}}36^{\text{m}}12^{\text{s}}.744$. This position was carefully chosen to optimize the IFU bundle mapping of desired targets. The first two plates were observed in Spring, 2015. The third to fifth plates were observed in Spring, 2016. The sixth plate was observed in Spring, 2017. The total on-source exposure time in each plate is 2.25 hr. To evaluate the impact on low surface brightness targets from systematic residuals (see Section 2.3), we have shuffled the IFU bundles used for the same target among different plates. The most frequently used IFU bundles for UDGs are 61-fiber bundles, but 37-fiber bundles and 91-fiber bundles have been used to observe them as well. The stacked spectra in our analyses are from the inner 19 fibers of each bundle for the optimum integrated signal-to-noise ratio (S/N). The locations of the stacked region for the three UDGs analyzed in this paper are shown in Figure 1. The diameter of each stacked region on

¹⁹ <http://www.sdss.org/dr14/manga/manga-target-selection/ancillary-targets/coma/>

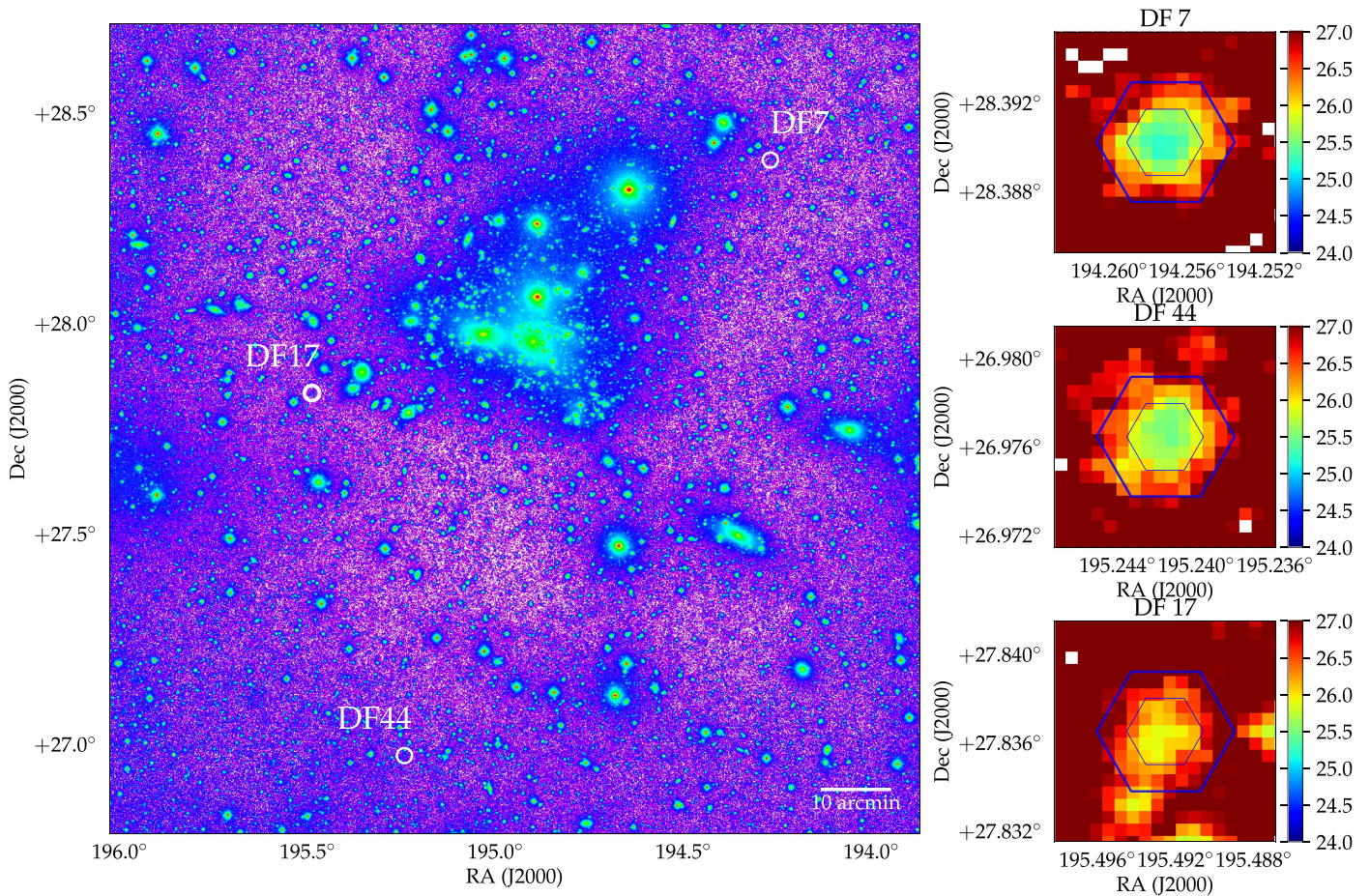


Figure 1. Left panel: overview of the MaNGA fiber bundle locations of three UDGs on the g -band surface brightness map of the Coma cluster. The image is from the Dragonfly Telephoto Array. Three white circles show the locations of DF 7, DF 44, and DF 17 but are not true to the IFU size. Right panels: zoomed-in g -band surface brightness map of three UDGs. Large hexagons show the footprints of MaNGA 61-fiber IFUs, and small hexagons show the stacked regions (19 fibers). Colorbars show the surface brightness in the g -band.

the sky is $12''.5$. The positions, central surface brightness, and effective radii of the two UDGs are shown in Table 1. The stacked regions sample roughly the inner 0.7 effective radii of the three UDGs.

To probe low surface brightness regions, excellent sky subtraction is required. In the Deep Coma plates, the locations of the reference sky fibers are carefully selected using images from the Dragonfly Telephoto Array. The expected g -band surface brightness of all-sky fiber locations (~ 3 arcsec around each fiber) based on the Dragonfly imaging are > 27.8 mag arcsec $^{-2}$. In addition to the 92 single fibers used to construct the model sky spectrum for ordinary MaNGA plates, we also devote three IFU bundles (two 19-fiber bundles, one 37-fiber bundle) to additional measurements of the sky. These additional sky fibers enable us to reach fainter surface brightness limits for stacked spectra than the regular MaNGA survey. The 1σ limiting surface brightness we are able to detect is calculated from the 1σ rms in the wavelength range of 4000–5500 Å, and is 27.6 mag arcsec $^{-2}$ for the Deep Coma plates.

To further improve the accuracy of the background estimate and to mitigate systematics, we adopt an on-and-off nodding strategy. The goal is to obtain reference “all-sky” exposures by shifting the whole field approximately $20'$ away, so that most of the sky fibers and science IFUs will sample the blank sky. We searched for the ideal locations for the shifts using

images from the Dragonfly Telephoto Array to optimize the fraction of both the science and sky fibers on the low surface brightness region. Each of the first two plates includes nine 5-minute nodding exposures at nine different locations between the normal science exposures. Each of the last four plates includes four 15-minute nodding exposures at four different locations.

2.3. Data Reduction

We processed our data using version 2_2_0 of the MaNGA Data Reduction Pipeline (DRP; Law et al. 2015, 2016). This version is similar to v2_1_2 released in 2017 July as SDSS DR14 (Abolfathi et al. 2018), but incorporates a number of custom modifications made specifically for the Deep Coma program. The baseline DRP first removes detector overscan regions and quadrant-dependent bias and extracts the spectrum of each fiber using an optimal profile-fitting technique. It next uses the sky fibers to create a super-sampled model for the background sky spectrum and subtracts this model spectrum from each of the science fibers. Flux calibration is then performed on individual exposures using 12 seven-fiber IFUs targeting spectrophotometric standard stars (Yan et al. 2016b). Fiber spectra from the blue and red cameras are then combined together onto a common logarithmic wavelength solution using a cubic b-spline fit. These “mgCFRAME” files thus represent

Table 1
UDG Properties

Target	DF 7	DF 44	DF 17
α	12 ^h 57 ^m 01. ^s 7	13 ^h 00 ^m 58. ^s 0	13 ^h 01 ^m 58. ^s 3
δ	28°23′25″	26°58′35″	27°50′11″
$\mu_{0,g}$ (mag/arcsec ⁻²)	24.4 ± 0.5	24.5 ± 0.5	25.1 ± 0.5
M_g (mag)	-16.0 ^{+0.2} _{-0.2}	-15.7 ^{+0.2} _{-0.2}	-15.2 ^{+0.3} _{-0.2}
R_{eff} (kpc)	4.3 ^{+1.4} _{-0.8}	4.6 ^{+1.5} _{-0.8}	4.4 ^{+1.5} _{-0.9}
S/N (4500–5000 Å)	9.5 Å ⁻¹	7.9 Å ⁻¹	5.0 Å ⁻¹
Constraints from Spectra			
Velocity (km s ⁻¹)	6600 ⁺⁴⁰ ₋₂₆	6402 ⁺⁴¹ ₋₃₈	8311 ⁺⁴³ ₋₄₃
log(age/Gyr)	0.93 ^{+0.17} _{-0.18}	1.02 ^{+0.11} _{-0.24}	0.88 ^{+0.22} _{-0.42}
[Fe/H]	-1.03 ^{+0.31} _{-0.34}	-1.25 ^{+0.33} _{-0.39}	-0.83 ^{+0.56} _{-0.51}
(M/L) _r	1.63 ^{+0.55} _{-0.29}	1.86 ^{+0.39} _{-0.56}	1.54 ^{+0.71} _{-0.52}
log(M_*/M_\odot)	8.74 ^{+0.17} _{-0.11}	8.66 ^{+0.12} _{-0.15}	8.42 ^{+0.22} _{-0.19}
Combined Constraints from Spectra and Photometry			
Velocity (km s ⁻¹)	6599 ⁺⁴⁰ ₋₂₅	6402 ⁺⁴¹ ₋₃₉	8315 ⁺⁴³ ₋₄₃
log(age/Gyr)	0.90 ^{+0.17} _{-0.16}	0.95 ^{+0.17} _{-0.20}	0.96 ^{+0.16} _{-0.40}
[Fe/H]	-1.04 ^{+0.32} _{-0.36}	-1.25 ^{+0.35} _{-0.41}	-0.80 ^{+0.49} _{-0.47}
(M/L) _r	1.56 ^{+0.47} _{-0.28}	1.64 ^{+0.54} _{-0.38}	1.80 ^{+0.51} _{-0.66}
log(M_*/M_\odot)	8.72 ^{+0.17} _{-0.13}	8.61 ^{+0.16} _{-0.11}	8.49 ^{+0.15} _{-0.20}

Note. We adopt the locations, central g -band surface brightness, absolute g -band magnitude and effective radii from van Dokkum et al. (2015a). Stellar population properties are derived from the central 19 fibers.

spectra of all 1423 MaNGA fibers from a single exposure in a row-stacked format, where each row corresponds to an individual one-dimensional fiber spectrum. The logarithmic wavelength grid runs from $\log \lambda(\text{Å}) = 3.5589$ to $\log \lambda(\text{Å}) = 4.0151$, which corresponds to 4563 spectral elements from 3621.5960 to 10353.805 Å. We do not utilize the 3D stage DRP (which combines fiber spectra into three-dimensional data cubes), and restrict our analysis to the mgCFRAME row-stacked spectra.

A number of custom modifications were made to the DRP in v2_2_0 to optimize performance for observations of low surface brightness regions in the Coma cluster. First, the DRP was modified to use the 167 total sky fibers (92 single fibers plus 3 IFU fiber bundles) to construct the model sky spectrum. Second, analysis of our nodded all-sky observations showed evidence for low-level systematics in the detector electronics. We added a step in the pipeline to measure and remove a 0.5 e-/pixel offset in bias between the light-sensitive detector pixels and the overscan region, compensating at the same time for a seasonally dependent 0.1 electron/pixel drift in the difference. Additionally, we found that the amplifier-dependent gain values tended to drift from one exposure to the next away from nominal at the $\sim 0.1\%$ level; we added procedures to measure and correct for this effect empirically using the sky fibers in each exposure. Finally, we modified the DRP to be able to apply the flux calibration vector from the nearest (in time) ordinary science exposure to the nod exposures (for which there are no calibration stars in the 7-fiber mini bundles).

Additionally, performance analysis of early observations in the Deep Coma program revealed that scattered light and the extended (>100 pixel) profile wings of bright galaxies targeted by the Coma program were contaminating the spectra of fainter objects. We therefore redesigned our observing program to

consolidate all bright targets (central and dE galaxies) onto one of the two BOSS spectrographs, and all faint targets (UDGs and intracluster light) onto the other so that these targets never share a detector.

Although these modifications substantially improve performance for the Deep Coma program relative to the DR14 baseline DRP, we find that the final stacked science spectra are nonetheless still limited by systematic residuals over large wavelength scales (>100 Å). These residuals are consistent between stacked science and nodded sky spectra within each plate, possibly due to cartridge-dependent uncertainties in fiber alignment and the detector point-spread function. For example, in the fifth plate, the stacked science spectrum for DF 17 is systematically negative in flux, but the nodded sky spectrum is systematically more negative, and the offset ranges from 0 to 10^{-18} erg s⁻¹ cm⁻² Å⁻¹. In the last four plates, we mitigate the impact of these systematics by fitting the stacked spectra of the sky subtracted nodded sky exposures with a tenth degree polynomial from 3836 to 5873 Å in the observed frame and subtracting the result from the corresponding science exposures prior to stacking science spectra. The amplitude of polynomial correction ranges from 10^{-19} to 10^{-18} erg s⁻¹ cm⁻² Å⁻¹ in the continuum and represents an important correction to the baseline flux level for extremely faint targets. We manage to match the continuum levels of stacked spectra from different plates via subtracting the above polynomial continuum before we derive any science result.

The mean S/N we achieved after all of these steps was 9.5 Å⁻¹ for DF 7, 7.9 Å⁻¹ for DF 44, and 5.0 Å⁻¹ for DF 17 in the observed wavelength range of 4500–5000 Å. This corresponds to a total integration time on source of 13.5 hr, and a total integration time on nod exposures of 4 hr.

3. Stellar Population Modeling

3.1. Absorption Line Fitter

Our main tool for modeling spectra of galaxies and UDGs in our sample is the absorption line fitter (`alf`; Conroy & van Dokkum 2012a; Conroy et al. 2014, 2017). `alf` enables stellar population modeling of the full spectrum for stellar ages >1 Gyr and for metallicities from approximately -2.0 to $+0.25$. With `alf`, we explore the parameter space using a Markov Chain Monte Carlo algorithm (`emcee`, Foreman-Mackey et al. 2013). The program now adopts the MIST stellar isochrones (Choi et al. 2016) and utilizes a new spectral library that includes continuous wavelength coverage from 0.35 to 2.4 μm over a wide range in metallicity. This new library, described in Villaume et al. (2017), is the result of obtaining new IRTF NIR spectra for stars in the MILES optical spectral library (Sánchez-Blázquez et al. 2006). Finally, theoretical response functions, which tabulate the effect on the spectrum of enhancing each of the 18 individual elements, were computed using the ATLAS and SYNTH programs (Kurucz 1970, 1993). Further details of these updates to `alf` are described in Conroy et al. (2018). With `alf`, we are able to fit a two burst star formation history, the redshift, velocity dispersion, overall metallicity ($[Z/H]$), 18 individual element abundances, several IMF parameters, and a variety of “nuisance” parameters.

Throughout this paper, we use `alf` in a simplified mode. Not all the parameters are included, but only the recession velocity, age, overall metallicity $[Z/H]$ and abundances of Fe,

C, N, O, Mg, Si, Ca, Ti, and Na. The IMF is fixed to the Kroupa (2001) form. Instead of adopting a two burst star formation history in the standard model, the simplified mode adopts only a single-age component. We adopt this approach due to the limited S/N of the data. The intrinsic velocity dispersions of UDGs (van Dokkum et al. 2016) are assumed to be lower than both the instrumental resolution (Law et al. 2016) and the resolution of models. Therefore, we smoothed each spectrum based on the instrumental resolution of the corresponding fiber. The desired velocity resolutions (σ_D) are chosen based on the maximum instrumental resolution (maximum σ_i) and are different among three galaxies. The desired velocity resolutions are 110 km s^{-1} for DF 7, 125 km s^{-1} for DF 44, and 135 km s^{-1} for DF 17. Each spectrum is smoothed to the desired velocity resolution by convolving a wavelength dependent Gaussian kernel with $\sigma = \sqrt{\sigma_D^2 - \sigma_i^2}$. With `alf`, we fit for the velocity dispersion of the smoothed spectra and describe this property below as “resolution.” We adopt flat priors from 500 to $10,500 \text{ km s}^{-1}$ for recession velocity, 10 – 500 km s^{-1} for resolution, 1.0 – 14 Gyr for age, and -1.8 – $+0.3$ for $[\text{Fe}/\text{H}]$. The priors are zero outside of these ranges. For each spectrum, we fit a continuum in the form of a polynomial to the ratio between model and data. The polynomial order is $(\lambda_{\text{max}} - \lambda_{\text{min}})/100 \text{ \AA}$. During each likelihood call, the polynomial divided input spectrum and model are matched. For computational convenience, the continuum normalization occurs in two separate wavelength intervals, 3800 – 4700 \AA and 4700 – 5700 \AA (Conroy & van Dokkum 2012b). In this paper, we only use the data taken by the blue spectrograph. This allows us to avoid additional issues associated with the numerous bright atmospheric OH features in the red. Pixels near bright sky lines in the blue were masked prior to the fitting.

3.2. Mock Data Tests

In this section, we examine how well the recession velocity, age, and $[\text{Fe}/\text{H}]$ can be recovered with `alf`. We have constructed a mock spectra data set with 20 realizations at a range of S/Ns from 5 to 50 \AA^{-1} . We assume that the mock spectra have a true recession velocity of 7200 km s^{-1} , a velocity dispersion of 50 km s^{-1} and a metallicity of $[\text{Fe}/\text{H}] = -0.8$. We test a set of mock spectra with ages of 10 Gyr and the other with ages of 3 Gyr. The data are fit over two wavelength ranges, 3800 – 4700 \AA and 4700 – 5700 \AA . The fitting ranges are the same as what we apply to the UDG spectra. In addition, the mock spectra are convolved by a 100 km s^{-1} Gaussian kernel since we need to smooth the UDG spectra. The results are shown in Figure 2 as a function of S/N.

The S/N of our UDG spectra lie between 5 and 10. From the mock test of the old stellar population, we estimate that their recession velocities, $\log(\text{age}/\text{Gyr})$, and $[\text{Fe}/\text{H}]$ can be reliably measured with an uncertainty of 14 – 29 km s^{-1} , 0.14 – 0.22 , and 0.21 – 0.39 dex, respectively. From the mock test of the 3 Gyr stellar population, we estimate that their recession velocities, $\log(\text{age}/\text{Gyr})$, and $[\text{Fe}/\text{H}]$ can be reliably measured with an uncertainty of 16 – 36 km s^{-1} , 0.14 – 0.23 , and 0.31 – 0.52 dex, respectively. The recession velocity can be recovered at a good accuracy for mock spectra at all S/Ns. The bias in the recovered parameter is small even at low S/N: for $\log(\text{age}/\text{Gyr})$ and $[\text{Fe}/\text{H}]$, the bias is of the order of 0.01 – 0.04 and 0.05 – 0.12 dex, well within the statistical uncertainties.

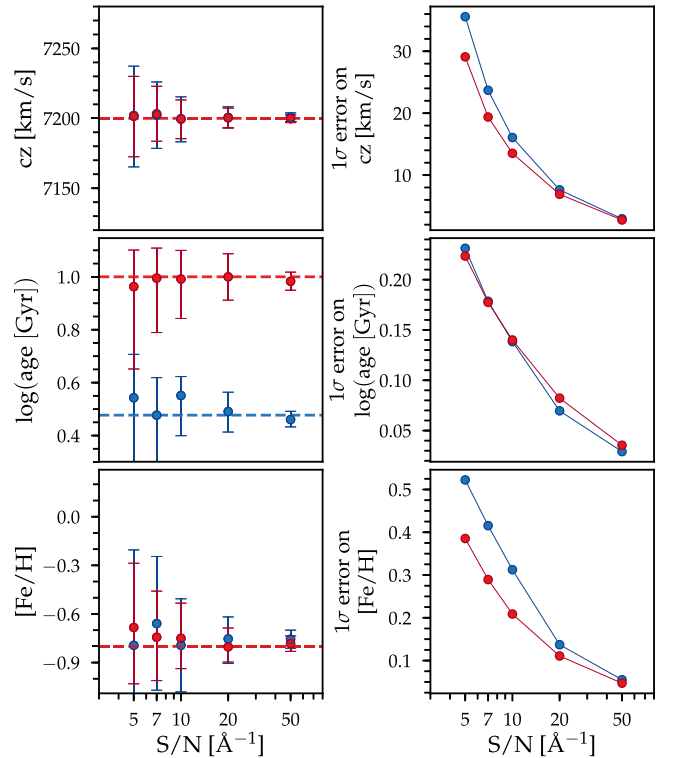


Figure 2. Test of the recovery of recession velocity, age, and $[\text{Fe}/\text{H}]$ with mock spectra as a function of S/N. We constructed 20 realizations at S/N of 5, 7, 10, 20, and 50 \AA^{-1} . The different colors represent mock spectra with different stellar ages, where the blue and red represent models with ages of 3 Gyr and 10 Gyr, respectively. Left panels: true values are shown as horizontal dashed lines. Circles, and lower and upper error bars show the mean values of the 50th, 16th, and 84th percentile of the posterior distributions of 20 realizations. Right panels: 1σ uncertainties of recession velocity, $\log(\text{age}/\text{Gyr})$, and $[\text{Fe}/\text{H}]$ as a function of S/N, averaged over the 20 realizations.

4. Results

We now present our results from full spectral modeling. A summary of the available information of the three targets is provided in Table 1, including their locations, g -band central surface brightness, effective radii (van Dokkum et al. 2014), mean S/N of the spectra, and derived stellar population properties.

4.1. Stellar Populations for DF 7, DF 44, and DF 17

In this section, we present our constraints on the redshift, age, and metallicity for DF 7 (Figures 3 and 4), DF 44 (Figures 5 and 6), and DF 17 (Figures 7 and 8). For each parameter, we present the median values and the 16th and 84th percentile of the posterior distributions. Top panels of Figures 3, 5, and 7 show the normalized median stacked spectra of DF 7, DF 44, and DF 17 with the inner 19 fibers over all exposures in black, and our best-fit model spectra in red. The best-fit model spectra are generated with parameters at the minimum χ^2 .

The bottom panels of Figures 3, 5, and 7 show the fractional residuals in black, compared with flux uncertainty in the yellow shaded regions. The comparison between the residual and data uncertainty indicates that the fitting results for all three UDGs are successful, as the residuals are all consistent with the flux uncertainty. For DF 7 and DF 44, several prominent absorption line features that are well-known for estimating stellar age and metallicity, such as $\text{H}\delta$, $\text{H}\gamma$, $\text{H}\beta$, $\text{Mg } b$, and the G -band at

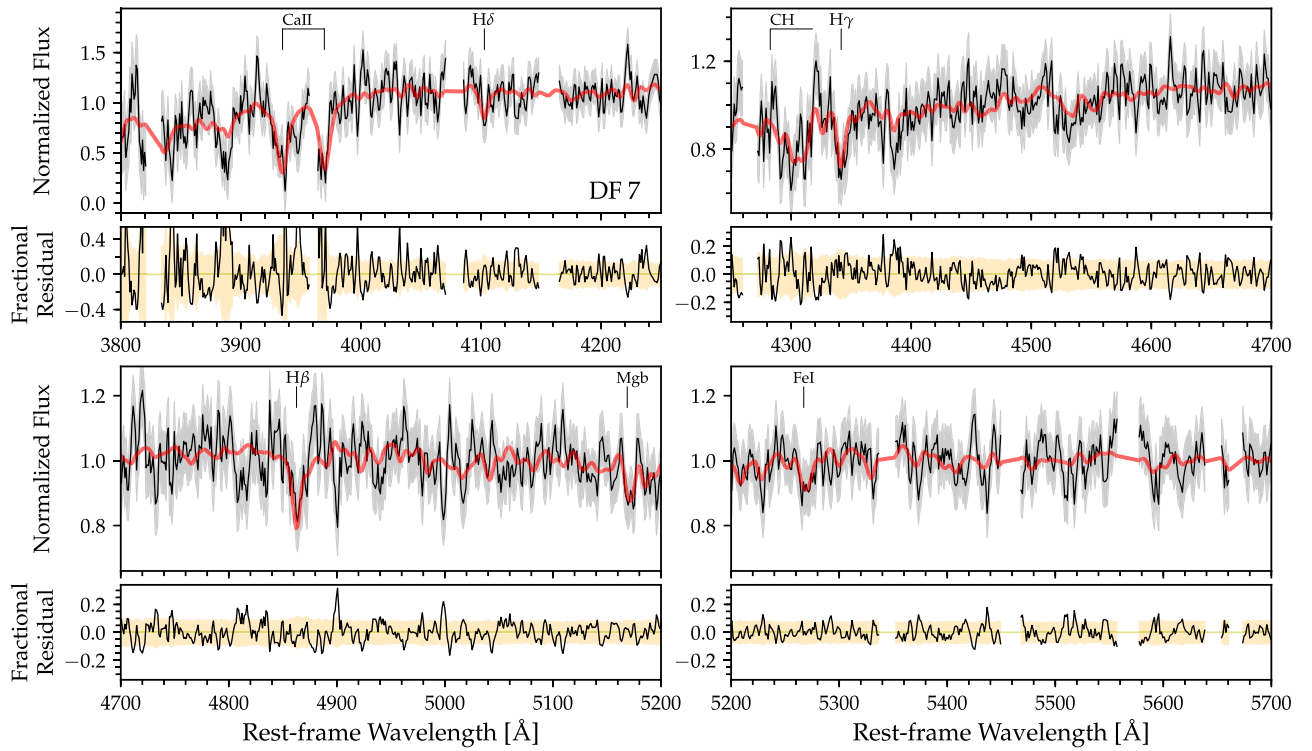


Figure 3. Top panel: stacked spectrum of DF 7 (black) and best-fit model spectrum (red) with parameters at minimum χ^2 from `alf`. Gray shaded regions show the uncertainty of flux from the input spectrum. Bottom panel: fractional residuals (black) are compared with the uncertainty of flux from the input spectrum (yellow). Gaps in the black lines indicate pixels that are masked prior to the fitting, which are pixels under the bright sky lines.

~ 4300 Å are all well described by the best-fit model. The Ca II H and K lines are very prominent as well. The spectrum for DF 17 has a much lower S/N, but key features such as H γ and H β are all clearly visible and well described by the best-fit model.

In Figures 4, 6, and 8, we show the projections of posteriors for several parameters we fit in `alf`, including the recession velocity, $\log(\text{age}/\text{Gyr})$, and $[\text{Fe}/\text{H}]$ (Foreman-Mackey 2016). As described in Section 2, the input spectra have been smoothed to the desired velocity resolutions, which are 110 km s^{-1} for DF 7, 125 km s^{-1} for DF 44, and 135 km s^{-1} for DF 17. Therefore, when we fit the spectra with `alf`, the velocity dispersion of our model spectra cannot be taken as a description of the intrinsic velocity dispersion of our targets. To avoid confusion, we describe this property as “resolution” in Figures 4, 6, and 8. Although we do not attempt to derive reliable velocity dispersion from the smoothed spectra, it is reassuring to see that the resolution we derive is roughly consistent with the sum in quadrature of the measured velocity dispersion from van Dokkum et al. (2016) and the desired resolution. For all derived parameters, the values of parameters at 16th, 50th, and 84th percentiles of posteriors are shown as dashed lines in the 1D histograms and contours in the 2D histograms. Outliers are shown as dots. The blue lines in the 2D histograms mark the values of parameters at minimum χ^2 .

We find that the recession velocities of DF 7, DF 44, and DF 17 are $6600^{+40}_{-26} \text{ km s}^{-1}$, $6402^{+41}_{-39} \text{ km s}^{-1}$, and $8311^{+43}_{-43} \text{ km s}^{-1}$. The uncertainties are consistent with the mock data tests. For DF 44, our result is consistent with the recession velocity measured by van Dokkum et al. (2016, 2017). They measured the kinematics of DF 44 using a 33.5 hr integration spectra observed by the DEIMOS spectrograph on the Keck II telescope,

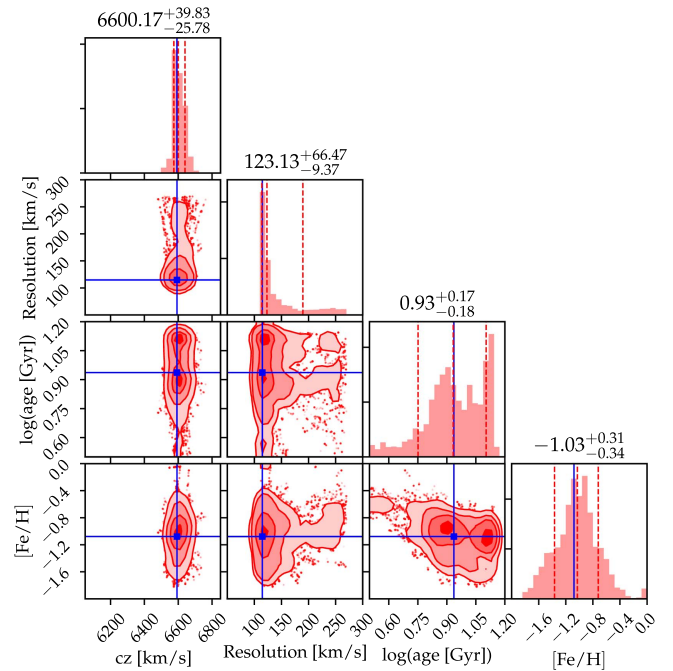


Figure 4. Projections of the posterior of recession velocity, $\log(\text{age})$, and $[\text{Fe}/\text{H}]$ from `alf` in 1D and 2D histograms for DF 7. Dashed lines in 1D histograms and contours in 2D histograms show the 16th, 50th, and 84th percentiles of posteriors. Blue lines represent the best-fit parameters at minimum χ^2 , which are used to generate best-fit model spectra.

and obtained a recession velocity of $6398^{+6} \text{ km s}^{-1}$ for DF 44. The recession velocity of DF 7 is consistent with the measurement by Kadowaki et al. (2017, $cz = 6587 \pm 33 \text{ km s}^{-1}$). The derived

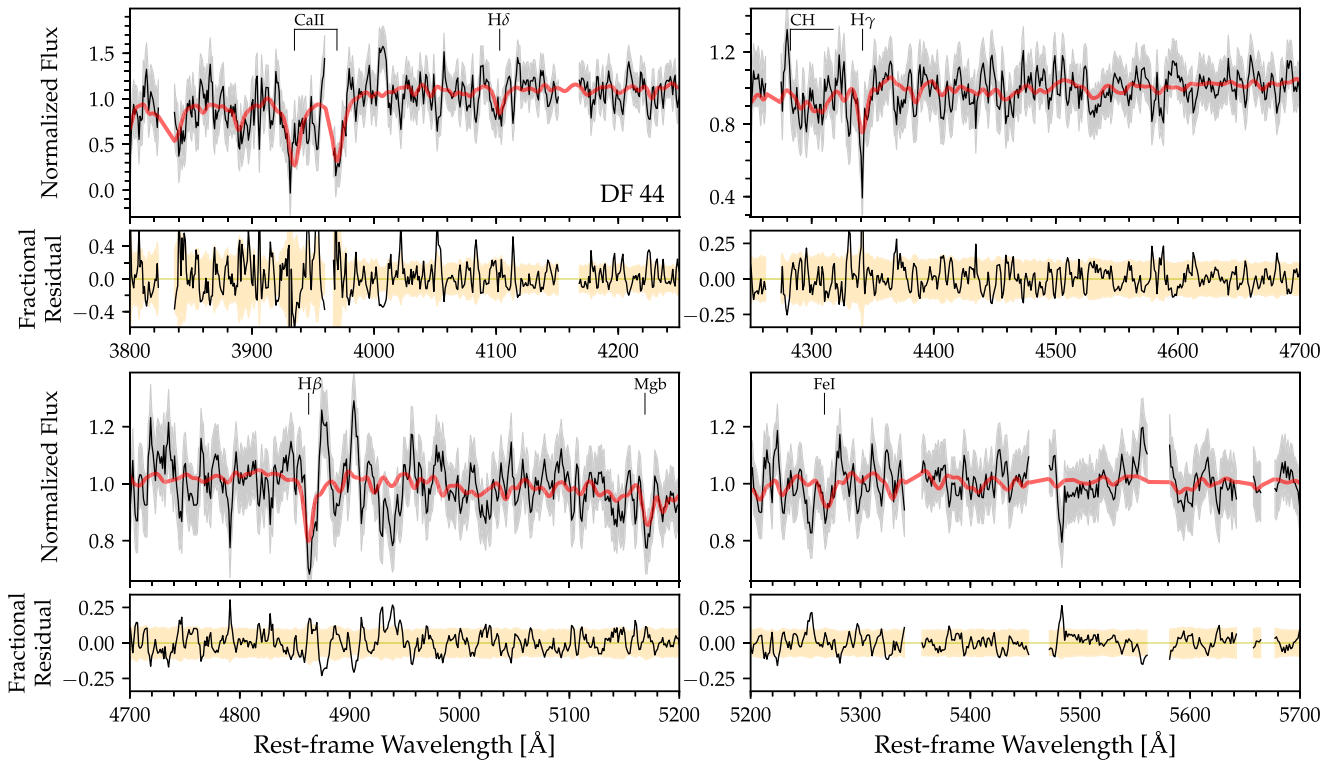


Figure 5. Same as Figure 3, but for DF 44.

recession velocities confirm that all of the three UDGs are members of the Coma cluster.

The ages of DF 7, DF 44, and DF 17 are $8.57^{+4.11}_{-2.93}$ Gyr, $10.50^{+3.00}_{-4.39}$ Gyr, and $7.61^{+5.09}_{-4.72}$ Gyr. The iron abundances, $[\text{Fe}/\text{H}]$, are $-1.03^{+0.31}_{-0.34}$, $-1.25^{+0.33}_{-0.39}$, and $-0.83^{+0.56}_{-0.51}$, respectively. The uncertainties of both $\log(\text{age}/\text{Gyr})$ and $[\text{Fe}/\text{H}]$ are similar to what was derived from the mock tests. From the 2D posterior distributions in Figures 4, 6, and 8, one can see that there are no strong degeneracies between the resolution and age or metallicity. There is a modest degeneracy between age and metallicity, as expected (Worthey 1994). The age posteriors are not perfectly Gaussian, but the local maximum in the marginalized age posteriors are all in the old age regime. The probabilities that the stellar populations are young are very low. The 16th percentiles of age posteriors are 5.6, 6.0, and 2.9 Gyr, and the 2.5th percentiles of age posteriors are 2.6, 2.7, and 1.4 Gyr for DF 7, DF 44, and DF 17, respectively. In addition, the mock test shows that `alf` is able to recover the true ages for young (3 Gyr) stellar populations. The primary result of this paper is that all three UDGs are old and metal-poor.

4.2. Combined Constraints from Spectra and Photometry

In this section, we add the $g-r$ color as an additional constraint to our stellar population parameters. We measure the color from the Dragonfly data within an aperture of $6''$, which is similar to the regions of our stacked spectra. The measured $g-r$ colors are 0.57 ± 0.05 mag, 0.53 ± 0.05 mag, and 0.65 ± 0.06 mag, respectively. In Figure 9, the normalized 1D posterior distributions of the $g-r$ color derived from fitting the continuum-normalized spectra are shown in the top panels in black. We assume the probability density of the observed $g-r$ colors to be a normal distribution and take the measured color and uncertainty as the mean and standard deviation of this

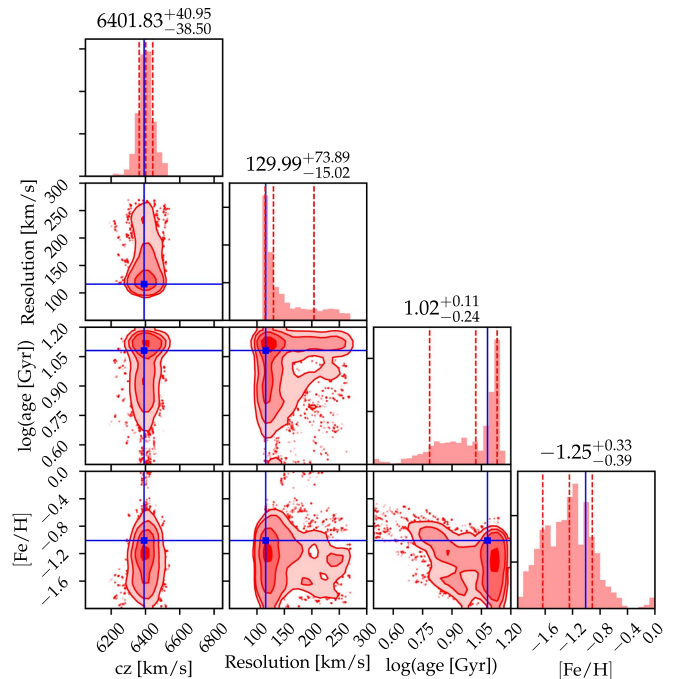


Figure 6. Same as Figure 4, but for DF 44.

normal distribution. The top panels show that the differences between the observed color and the inferred color from the models are no more than 0.02 mag for both DF 7 and DF 44. The good agreement between the inference from fitting spectra and the observed colors suggests that reddening is low in both UDGs, and therefore their gas and dust content is likely low. For DF 17, the color from photometry is slightly redder than the color from the spectral models, but the difference is smaller

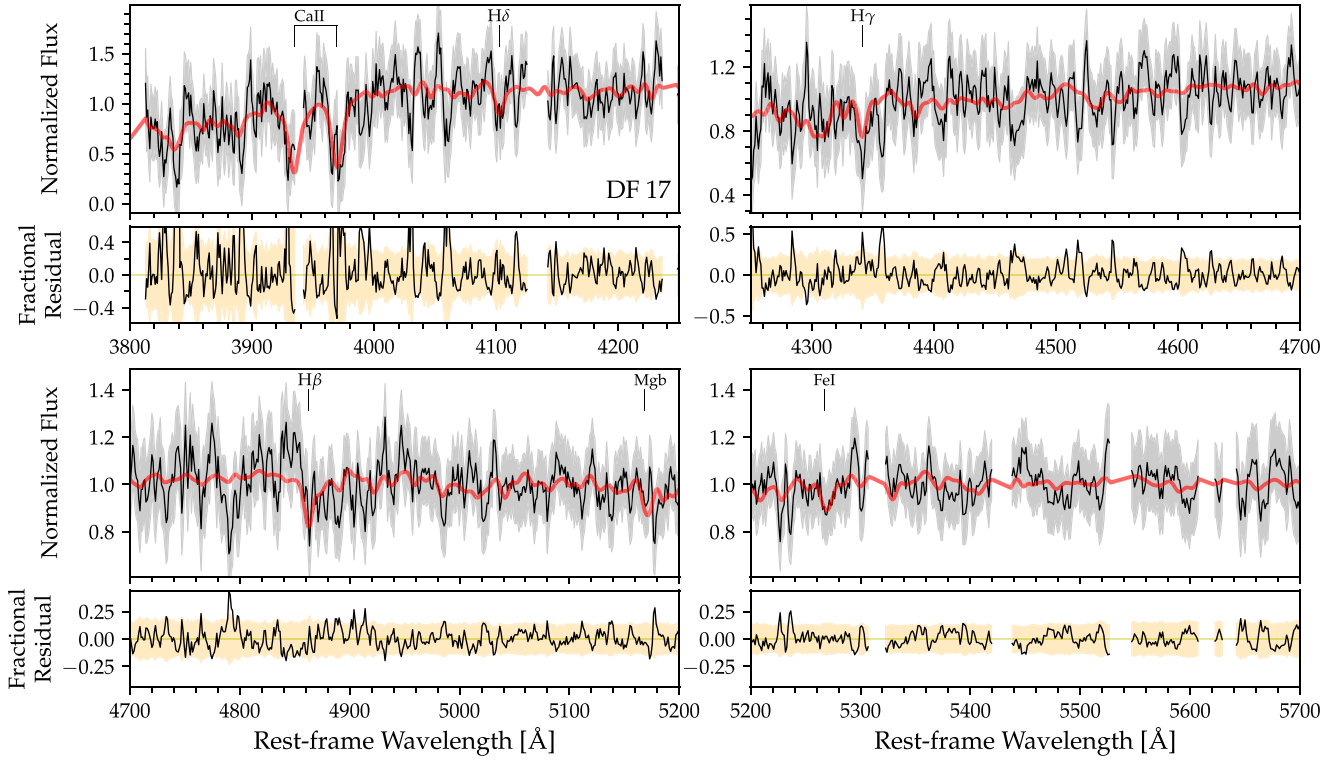


Figure 7. Same as Figure 3, but for DF 17.

than 1σ uncertainty. Near-infrared photometry would be helpful to confirm whether DF 17 is dust reddened.

We use the observed $g-r$ color to further constrain the model space. We re-weight the MCMC chains based on the probability density of the broadband $g-r$ color, and generate new posterior distributions by bootstrap resampling. The middle and bottom panels of Figure 9 show the joint posterior distributions of $\log(\text{age}/\text{Gyr})$ and $[\text{Fe}/\text{H}]$ in red, respectively. Compared with the posterior distributions obtained from spectroscopy alone, we find that the inclusion of photometry results in slightly tighter constraints for DF 44 and DF 7. This is at least partially due to the relatively large errors on the observed colors—more precise colors would likely result in stronger constraints on the age and metallicity. The results from these joint constraints are also shown in Table 1. For DF 17, an additional constraint from photometry provides us with a slightly older and less metal-poor stellar population.

4.3. Stellar Mass

We calculate the stellar mass using the g -band total integrated magnitude from van Dokkum et al. (2014). The g -band integrated magnitudes for DF 7, DF 44, and DF 17 are $-16.0^{+0.2}_{-0.2}$ mag, $-15.7^{+0.2}_{-0.2}$ mag, and $-15.2^{+0.3}_{-0.2}$ mag. The $g-r$ color within $6''$ from the galaxy centers are 0.57 ± 0.05 mag, 0.53 ± 0.05 mag, and 0.65 ± 0.06 mag. We adopt the r -band solar absolute magnitude as 4.76 from Blanton et al. (2003). r -band K -corrections are calculated based on the best-fit model spectra, and $K_r \sim -0.02$. The rest-frame r -band mass-to-light ratio for DF 7, DF 44, and DF 17 are taken from the results constrained jointly by spectra and photometry within a radius of $6''$, and they are $1.56^{+0.47}_{-0.28} M_{\odot}/L_{\odot}$, $1.64^{+0.54}_{-0.38} M_{\odot}/L_{\odot}$, and $1.80^{+0.51}_{-0.66} M_{\odot}/L_{\odot}$. Therefore, the stellar masses for the three UDGs are $5.24^{+2.27}_{-1.22} \times 10^8 M_{\odot}$, $4.03^{+1.87}_{-1.05} \times 10^8 M_{\odot}$, and

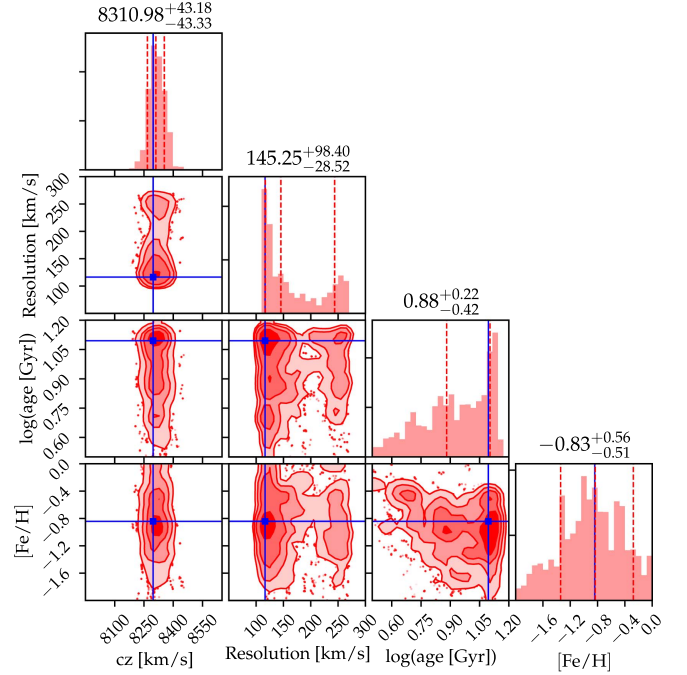


Figure 8. Same as Figure 4, but for DF 17.

$3.11^{+1.28}_{-1.15} \times 10^8 M_{\odot}$, respectively. van Dokkum et al. (2016) has calculated the stellar mass for DF 44 using its i -band luminosity and $g-i$ color. Our result is consistent with theirs ($M_{*} \approx 3 \times 10^8 M_{\odot}$).

5. Discussion

We have presented the first spectroscopic measurements of age and metallicity for three UDGs in the Coma cluster, DF 7,

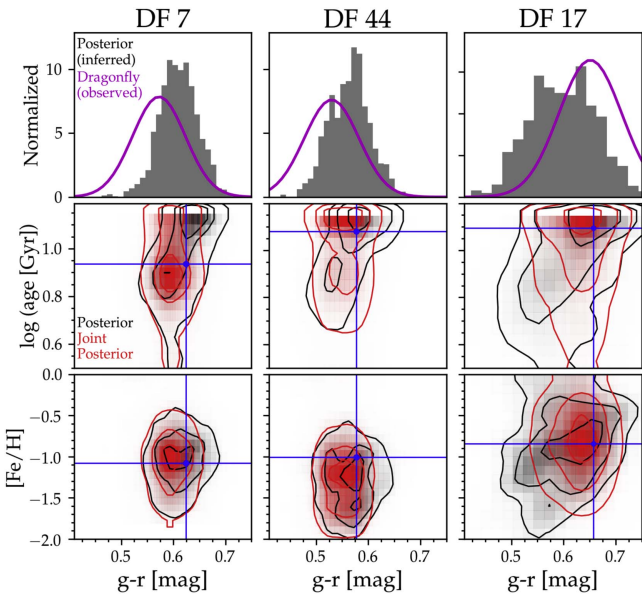


Figure 9. Top panels: 1D histogram of $g-r$ color posterior from `a1f` (gray) for DF 7 (left), DF 44 (middle), and DF 17 (right), compared with the $g-r$ color from broadband images taken by the Dragonfly Telephoto Array (purple). Middle and bottom panels: Projections of the posterior of $\log(\text{age})$, $[\text{Fe}/\text{H}]$, and $g-r$ in 2D histograms (black). Contours show the 16th, 50th, and 84th percentile. Blue lines show the best-fit parameters at minimum χ^2 . The joint posterior distributions from combining broadband colors and model spectra colors are shown in the same panels in red.

DF 44, and DF 17. In addition, we have presented the first spectroscopic redshift for DF 17. These three UDGs are among the brightest and largest UDGs in the sample of van Dokkum et al. (2015a). We find that all of the three UDGs are old ($7.94^{+3.60}_{-2.49}$ Gyr, $8.92^{+4.25}_{-3.26}$ Gyr, and $9.11^{+3.91}_{-5.54}$ Gyr), and metal-poor ($[\text{Fe}/\text{H}]_{\text{DF 7}} = -1.04^{+0.32}_{-0.36}$, $[\text{Fe}/\text{H}]_{\text{DF 44}} = -1.25^{+0.35}_{-0.41}$, $[\text{Fe}/\text{H}]_{\text{DF 17}} = -0.80^{+0.49}_{-0.41}$). Their stellar masses are $5.24^{+2.27}_{-1.22} \times 10^8 M_{\odot}$, $4.03^{+1.87}_{-1.05} \times 10^8 M_{\odot}$, and $3.11^{+1.28}_{-1.15} \times 10^8 M_{\odot}$, respectively. The results are summarized in Figure 10. The derived ages and metallicities are typical for low-mass galaxies in cluster environments (e.g., van Zee et al. 2004; Penny & Conselice 2008; Smith et al. 2009). Kadowaki et al. (2017) concluded that, on average, four Coma cluster UDGs in their sample are metal-poor by visually comparing the stacked spectrum against SSP models. The UDGs in our samples have metallicities consistent with this conclusion. Their ages are slightly older than early-type galaxies with similar or larger stellar masses. Their metallicities are broadly consistent with dwarf galaxies at similar stellar masses.

The ages of DF 7, DF 44, and DF 17 show that they all have old stellar populations, indicating that the star formation in all of the three galaxies must have been truncated at high redshift. In Figure 11, we show relationships between age, stellar mass, and velocity dispersion of the UDGs, and compare to other galaxies from the literature. The left panel shows three dwarf ellipticals in the Coma cluster obtained as part of the Deep Coma program (M. Gu et al., in preparation). Their stellar population properties are also derived from full optical spectral modeling with `a1f`. We also plot stellar properties of early-type galaxies from stacked SDSS spectra by Conroy et al. (2014). Among early-type galaxies, there is a weak trend such that less massive galaxies are slightly younger. In addition, we compare with a large magnitude-limited sample of SDSS galaxies from Gallazzi et al. (2005). Note that in their sample of

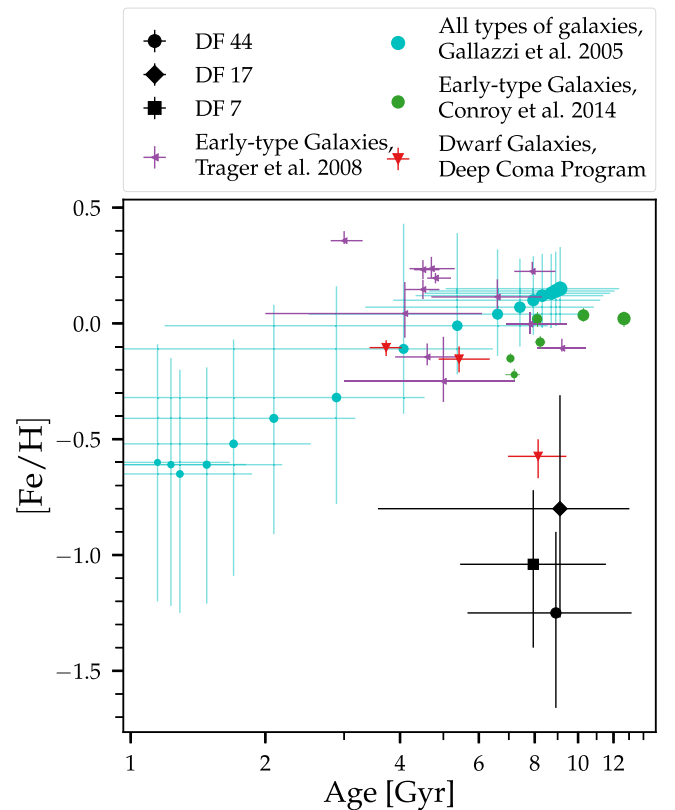


Figure 10. Relation between age and $[\text{Fe}/\text{H}]$ for DF 44, DF 7, and DF 17 (black), three dwarf elliptical galaxies in the Coma cluster (red, M. Gu et al., in preparation), and 12 early-type galaxies in the Coma cluster measured by Trager et al. (2008). In addition, cyan and green data points show the relation for various types of galaxies from Gallazzi et al. (2005), and early-type galaxies binned in stellar mass (Conroy et al. 2014) and Gallazzi et al. (2005), the sizes of data points represent different stellar masses of data bins, and they show a general trend that more massive galaxies are older and more metal-rich.

the low-mass galaxies are dominated by late-type galaxies and hence the mean ages are much younger.

In the right panel of Figure 11, we plot the relation between age and velocity dispersion. Thomas et al. (2010) studied a large sample of morphologically selected early-type SDSS galaxies. Caldwell et al. (2003) studied a sample including mostly low velocity dispersion ($\sigma < 100 \text{ km s}^{-1}$) early-type galaxies in the Virgo Cluster and in lower density environments. They found that there is a general trend that the galaxies with higher velocity dispersion are older. Trager et al. (2008) studied 12 early-type galaxies in the Coma cluster, including both elliptical and S0 galaxies. They seem to broadly obey the same (weak) relation. Both panels seem to suggest that, despite different techniques for estimating ages, there is a general trend that galaxies with higher stellar masses or larger velocity dispersions are older. Although the uncertainties are large, the three UDGs in this paper do not seem to fall on the same age–stellar mass trend. We only have velocity dispersion for DF 44 (van Dokkum et al. 2017, $\sigma = 47^{+8}_{-6} \text{ km s}^{-1}$). DF 44 also seems to be an outlier on the apparent age– σ trend. They are apparently older than dwarf elliptical and S0 galaxies at similar stellar mass and velocity dispersion in the Coma cluster (Trager et al. 2008).

The old ages indicate that the stellar components of large and diffuse galaxies such as DF 7, DF 44, and DF 17 can be formed at high redshift. Although we have only investigated three UDGs that are all at the high end of the UDG size

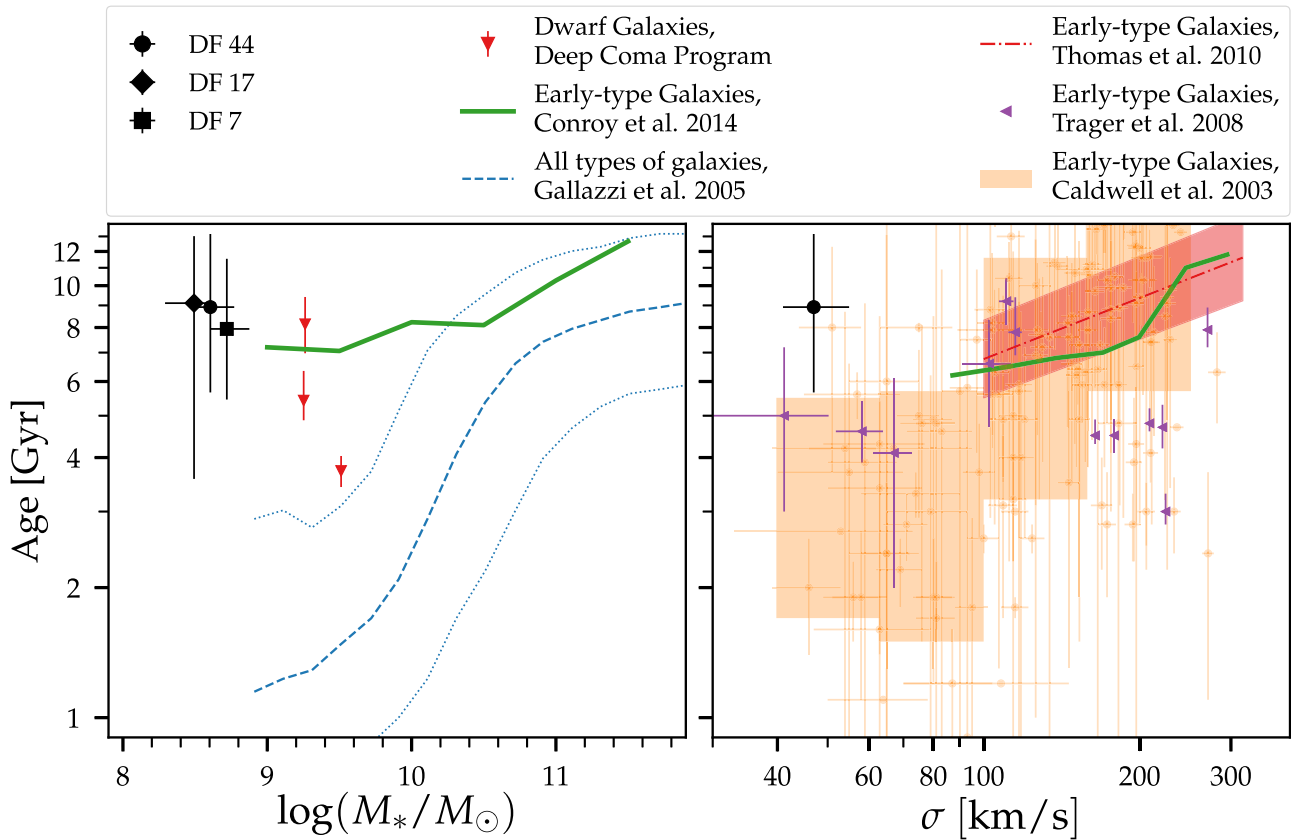


Figure 11. Relationship between age and stellar mass (left panel), and velocity dispersion (right panel). Our results are compared to three dwarf elliptical galaxies in the Coma cluster (red triangles, M. Gu et al., in preparation), early-type galaxies (Conroy et al. 2014) binned in stellar mass (left panel) and velocity dispersion (right panel), a sample of nearby early-type galaxies mostly with low-velocity dispersions (Caldwell et al. 2003), morphologically selected SDSS early-type galaxies (Thomas et al. 2010), SDSS galaxies covering a wide range of galaxy types (Gallazzi et al. 2005), and 12 early-type galaxies in the Coma cluster (Trager et al. 2008).

distribution, our results seem to rule out the scenario where UDGs recently quenched their star formation, for instance, due to recent accretion onto the Coma cluster. These results are also not consistent with the theoretical prediction that UDGs have a relatively late formation time compared to other low-mass galaxies (e.g., Rong et al. 2017). It is worth noting that our single-age assumption in the stellar population modeling is not enough to disentangle the full star formation history; future measurements of properties such as α -abundance will provide us with more information about the formation of UDGs.

Recent studies have shown that at least some of the UDGs have rich GC systems. Peng & Lim (2016) estimated that the number of GCs in DF 17 is 28 ± 14 , and van Dokkum et al. (2017) estimated that DF 44 hosts 74 ± 18 GCs. The specific frequency is $S_N = 26 \pm 13$ for DF 17 (Peng & Lim 2016), and $S_N = 27 \pm 7$ for DF 44 (van Dokkum et al. 2017). Since GCs are formed during early and rapid star formation, the relative higher specific frequency of GCs in these two UDGs may reflect that they have experienced intense starburst at high redshift (e.g., Liu et al. 2016). The old ages derived for DF 44 and DF 17 are consistent with this picture.

The relation between age and metallicity is shown in Figure 10. The three UDGs are compared with three dwarf elliptical galaxies in the Coma cluster, 12 early-type galaxies in the Coma cluster from Trager et al. (2008), massive early-type galaxies binned in stellar mass from Conroy et al. (2014), and SDSS galaxies covering a wide range of galaxy types from Gallazzi et al. (2005). For data from Conroy et al. (2014) and Gallazzi et al. (2005), the sizes of data points represent different

stellar masses of data bins, and they show a general trend that more massive galaxies are older and more metal-rich. The UDGs appear as outliers. Their low metallicities and old ages are consistent with a picture that their star formation histories are brief at high redshifts. Three dwarf elliptical galaxies in the Coma cluster appear to lie between UDGs and more massive galaxies. It would be interesting to look into the star formation and chemical enrichment histories of a larger sample of dwarf galaxies and UDGs in order to investigate whether there is any connection between these two properties.

The stellar mass–stellar metallicity relation (MZR) for galaxies provides important clues to their star formation and chemical enrichment history. The fact that this relation has relatively low scatter is a challenge to explain, especially at the low-mass end (e.g., Kirby et al. 2013). Previous work suggests that this relation is linked to the complex interplay between reionization, star formation, gas inflow, outflow, and recycling (e.g., Ma et al. 2016; Lu et al. 2017).

The top left panel of Figure 12 shows the locations of DF 7, DF 44, and DF 17 on the MZR relative to other populations, including dwarf galaxies in the Local Group (Kirby et al. 2013; gray dots), early-type galaxies stacked in stellar mass bins (Conroy et al. 2014) (green), star-forming galaxies in SDSS (Zahid et al. 2017), and the MZR from Gallazzi et al. (2005), which covers both star-forming and quiescent SDSS galaxies (light blue). We note that the data points from Zahid et al. (2017) and Gallazzi et al. (2005) in Figure 12 represent the total metallicities instead of iron abundances of galaxies in their samples. The large scatter of the MZR from Gallazzi et al.

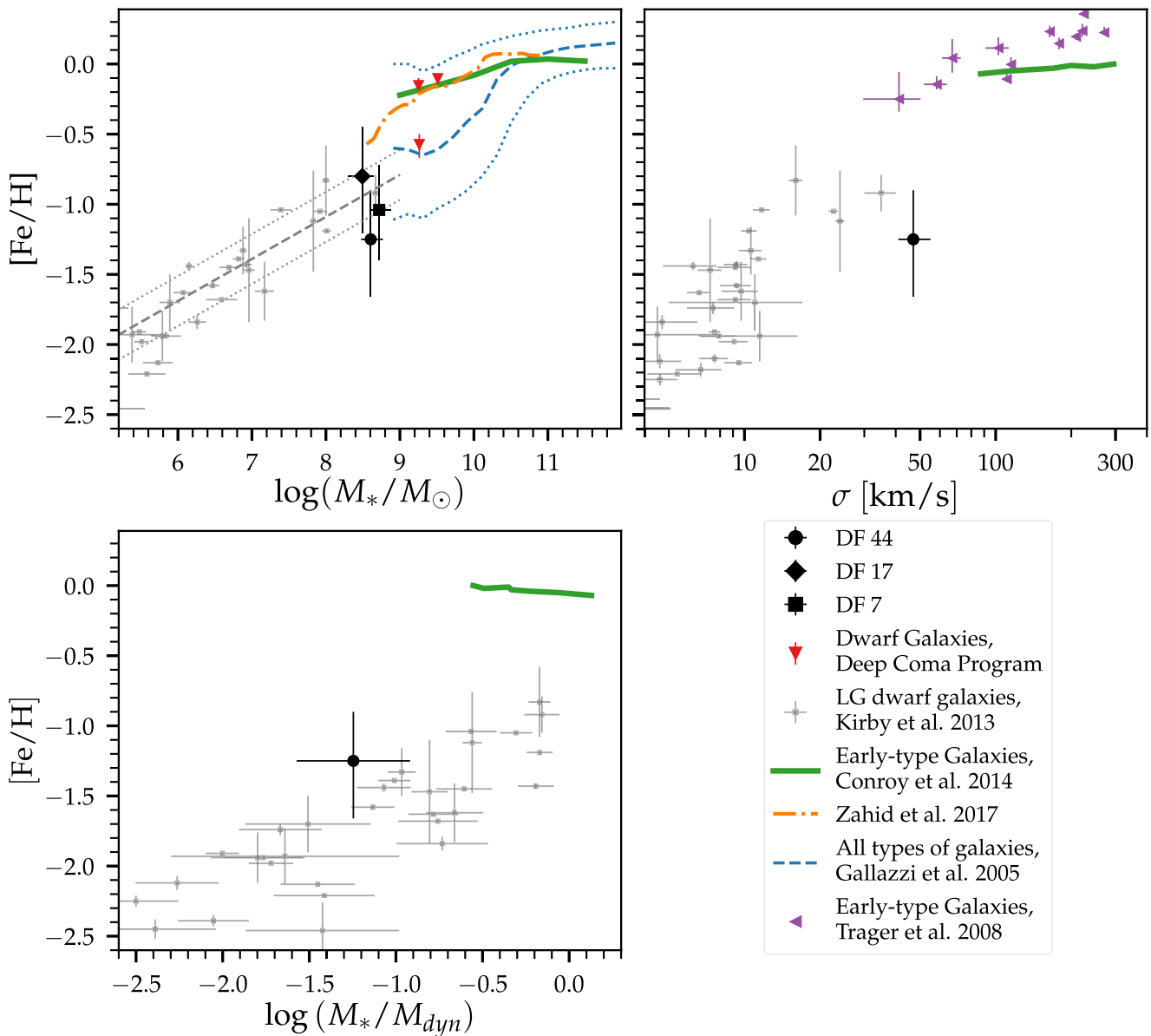


Figure 12. Top left: relation between stellar mass and $[Fe/H]$ for DF 44, DF 7, and DF 17 (black), compared with the stellar mass–stellar metallicity relation for three dwarf elliptical galaxies in the Coma cluster (triangles, M. Gu et al., in preparation), and previous results from the literature. Gray symbols show Local Group dwarf galaxies from Kirby et al. (2013), and gray dashed and dotted lines represent the median and 16th and 84th percentiles of the metallicity distributions. Cyan dashed and dotted lines show the median and 16th and 84th percentiles of the metallicity distributions for various types of galaxies in Gallazzi et al. (2005). Green symbols show the stellar mass–metallicity relation for early-type galaxies binned in stellar mass (Conroy et al. 2014). Top right: relation between velocity dispersion and $[Fe/H]$ for DF 44, compared with early-type galaxies binned in velocity dispersion (Conroy et al. 2014), and Local Group dwarf galaxies (Kirby et al. 2013). Bottom left: relation between metallicity and the logarithmic ratio of stellar mass to dynamical mass for DF 44, Local Group dwarf galaxies (Kirby et al. 2013) and early-type galaxies binned in velocity dispersion (Conroy et al. 2014).

(2005) is at least partially due to the mixture of both early- and late-type galaxies at lower masses combined with the increased difficulty of measuring stellar metallicities for star-forming galaxies. Considering that effect, the MZR seems to be continuous from low to high masses. Triangle symbols show three dwarf elliptical galaxies from our sample in the Coma cluster (M. Gu et al., in preparation), whose metallicities are generally consistent with the MZR from Kirby et al. (2013), Conroy et al. (2014), and Gallazzi et al. (2005). Despite the large uncertainties of metallicity and stellar mass, all of the three UDGs seem to follow the MZR defined by normal dwarf galaxies. This suggests that stellar mass plays an important role in determining stellar metallicities, regardless of a galaxy’s size.

Previous work concluded that some UDGs, including DF 44, may live in more massive dark matter halos than would be expected for their luminosities (e.g., $M_{vir} > 10^{11} M_\odot$, van Dokkum et al. 2016). In addition, it is well-known that the stellar properties of early-type galaxies are tightly related to their dynamical masses (e.g., Gallazzi et al. 2006; Graves et al. 2009). Therefore, we also look into the relation between their stellar properties and gravitational potential well depth. The top right panel of Figure 12 shows the relation between stellar velocity dispersion (σ) and metallicities. We compare DF 44 with dwarf galaxies (Kirby et al. 2013), massive early-type galaxies binned in velocity dispersion (Conroy et al. 2014). We also compare to 12 elliptical and S0 galaxies in the Coma cluster (Trager et al. 2008). Their iron

abundances are calculated based on their metallicities and the enhanced element abundances ($[Z/H]$ and $[E/Fe]$) in Trager et al. (2008) and Equation (3) in Trager et al. (2000). DF 44 stands out in this plot in the sense that it has lower metallicity for its σ compared to other galaxies. We also know that the stellar mass of DF 44 is unusually low for its σ and since it is the (massive) stars that produce metals, it is perhaps not surprising that DF 44 has low metallicity for its σ .

We explore this point further in the bottom-left panel of Figure 12, where we plot $[Fe/H]$ as a function of the logarithmic ratio of stellar mass to dynamical mass. This ratio is proportional to the integrated star formation efficiency. In this diagram, one can imagine diagonal tracks where a galaxy in a given halo evolves along the track as it converts baryons into stars. Tracks associated with more massive halos will be offset vertically in this diagram, as a given integrated star formation efficiency (a given stellar-to-dynamical mass ratio) will result in a higher stellar metallicity for galaxies in deeper potential wells, as such systems will be able to retain a greater fraction of the metals.

In this diagram, we compare the location of DF 44 to dwarf galaxies in the Local Group (Kirby et al. 2013) and massive early-type galaxies binned in velocity dispersion (Conroy et al. 2014). The dynamical masses of all galaxies in this panel are estimated using Equation (2) in Wolf et al. (2010) for dispersion-supported systems:

$$M_{\text{dyn}} = 4\sigma^2 R_e / G. \quad (1)$$

As anticipated, for a given stellar-to-dynamical mass ratio, galaxies in more massive halos have higher metallicities. DF 44 lies slightly above Local Group dwarf galaxies in this plot. Although the offset is marginal, it could be consistent with the idea that DF 44 is in an unusually massive dark matter halo for its stellar mass, which would allow this galaxy to retain a greater fraction of metals ejected from massive stars and hence result in a higher stellar metallicity. Further observations, including higher S/N spectra, will be necessary to make stronger conclusions.

Although DF 7, DF 44, and DF 17 reside in the inner regions of the Coma cluster, Figure 12 is not consistent with the picture that UDGs are tidal debris of more massive systems, unless the massive progenitors are true outliers of the stellar mass–stellar metallicity relation with high stellar masses and very metal-poor stellar populations. Also, their regular and smooth morphology do not show evidence of tidal disruption.

In this work, we have focused on three relatively luminous and large UDGs in the cluster environment. More data are needed on a wider variety of systems in order to make more general conclusions regarding the formation pathway(s) of UDGs.

6. Summary

We have presented the first stellar population analysis for three UDGs in the Coma cluster, DF 7, DF 44, and DF 17, based on the analysis of their optical spectra. We have measured their recession velocities, ages, metallicities, and stellar masses using spectra obtained as part of the Deep Coma Program within the SDSS-IV/MaNGA survey. We confirm that all of the three UDGs are members of the Coma cluster. They are all old and metal-poor, with ages of $7.94^{+3.60}_{-2.49}$ Gyr, $8.92^{+4.25}_{-3.26}$ Gyr, and

$9.11^{+3.91}_{-5.54}$ Gyr, and iron abundance of $[Fe/H] = -1.04^{+0.32}_{-0.36}$, $[Fe/H] = -1.25^{+0.35}_{-0.41}$, $[Fe/H] = -0.80^{+0.49}_{-0.47}$, respectively. Their stellar masses are $5.24^{+2.27}_{-1.22} \times 10^8 M_{\odot}$, $4.03^{+1.87}_{-1.05} \times 10^8 M_{\odot}$, and $3.11^{+1.28}_{-1.15} \times 10^8 M_{\odot}$. Their stellar populations are slightly older than early-type galaxies with similar or larger stellar mass and metallicity. Their metallicities are broadly consistent with known dwarf galaxies at similar stellar masses, but DF 44 falls below the $[Fe/H]$ – σ relation. In spite of their surprisingly diffuse structures and large sizes, it appears that their basic stellar population properties are not very atypical for their masses. These results disfavor UDG formation scenarios that predict late star formation and/or late quenching.











We thank the referee for helpful comments that improved this paper. M.G. acknowledges support from the National Science Foundation Graduate Research Fellowship. C.C. acknowledges support from NASA grant NNX15AK14G, NSF grant AST-1313280, and the Packard Foundation. M.B. acknowledges funding from NSF/AST-1517006. A.W. acknowledges support of a Leverhulme Trust Early Career Fellowship. The computations in this paper were run on the Odyssey cluster supported by the FAS Division of Science, Research Computing Group at Harvard University.

Funding for the Sloan Digital Sky Survey IV has been provided by the Alfred P. Sloan Foundation, the U.S. Department of Energy Office of Science, and the Participating Institutions. SDSS-IV acknowledges support and resources from the Center for High-Performance Computing at the University of Utah. The SDSS website is <http://www.sdss.org>.

SDSS-IV is managed by the Astrophysical Research Consortium for the Participating Institutions of the SDSS Collaboration including the Brazilian Participation Group, the Carnegie Institution for Science, Carnegie Mellon University, the Chilean Participation Group, the French Participation Group, Harvard-Smithsonian Center for Astrophysics, Instituto de Astrofísica de Canarias, The Johns Hopkins University, Kavli Institute for the Physics and Mathematics of the Universe (IPMU)/University of Tokyo, Lawrence Berkeley National Laboratory, Leibniz Institut für Astrophysik Potsdam (AIP), Max-Planck-Institut für Astronomie (MPIA Heidelberg), Max-Planck-Institut für Astrophysik (MPA Garching), Max-Planck-Institut für Extraterrestrische Physik (MPE), National Astronomical Observatories of China, New Mexico State University, New York University, University of Notre Dame, Observatório Nacional/MCTI, The Ohio State University, Pennsylvania State University, Shanghai Astronomical Observatory, United Kingdom Participation Group, Universidad Nacional Autónoma de México, University of Arizona, University of Colorado Boulder, University of Oxford, University of Portsmouth, University of Utah, University of Virginia, University of Washington, University of Wisconsin, Vanderbilt University, and Yale University.

ORCID iDs

Meng Gu  <https://orcid.org/0000-0002-4267-9344>
 Charlie Conroy  <https://orcid.org/0000-0002-1590-8551>
 David Law  <https://orcid.org/0000-0002-9402-186X>
 Pieter van Dokkum  <https://orcid.org/0000-0002-8282-9888>
 Renbin Yan  <https://orcid.org/0000-0003-1025-1711>
 David Wake  <https://orcid.org/0000-0002-6047-1010>
 Kevin Bundy  <https://orcid.org/0000-0001-9742-3138>
 Allison Merritt  <https://orcid.org/0000-0001-9467-7298>

Roberto Abraham  <https://orcid.org/0000-0002-4542-921X>
 Jielai Zhang  <https://orcid.org/0000-0001-5310-4186>
 Matthew Bershady  <https://orcid.org/0000-0002-3131-4374>
 Dmitry Bizyaev  <https://orcid.org/0000-0002-3601-133X>
 Jonathan Brinkmann  <https://orcid.org/0000-0001-6128-659X>
 Niv Drory  <https://orcid.org/0000-0002-7339-3170>
 Karen Masters  <https://orcid.org/0000-0003-0846-9578>
 Kaike Pan  <https://orcid.org/0000-0002-2835-2556>
 Anne-Marie Weijmans  <https://orcid.org/0000-0002-5908-6852>
 Kai Zhang  <https://orcid.org/0000-0002-9808-3646>

References

- Abolfathi, B., Aguado, D. S., Aguilar, G., et al. 2018, *ApJS*, 235, 42
 Abraham, R. G., & van Dokkum, P. G. 2014, *PASP*, 126, 55
 Amorisco, N. C., & Loeb, A. 2016, *MNRAS*, 459, L51
 Beasley, M. A., Romanowsky, A. J., Pota, V., et al. 2016, *ApJL*, 819, L20
 Beasley, M. A., & Trujillo, I. 2016, *ApJ*, 830, 23
 Bellazzini, M., Belokurov, V., Magrini, L., et al. 2017, *MNRAS*, 467, 3751
 Blanton, M. R., Bershady, M. A., Abolfathi, B., et al. 2017, *AJ*, 154, 28
 Blanton, M. R., Hogg, D. W., Bahcall, N. A., et al. 2003, *ApJL*, 592, 819
 Bothun, G. D., Impey, C. D., & Malin, D. F. 1991, *ApJL*, 376, 404
 Bundy, K., Bershady, M. A., Law, D. R., et al. 2015, *ApJL*, 798, 7
 Caldwell, N. 2006, *ApJL*, 651, 822
 Caldwell, N., Rose, J. A., & Concannon, K. D. 2003, *AJ*, 125, 2891
 Choi, J., Dotter, A., Conroy, C., et al. 2016, *ApJ*, 823, 102
 Colless, M., & Dunn, A. M. 1996, *ApJL*, 458, 435
 Collins, M. L. M., Chapman, S. C., Rich, R. M., et al. 2013, *ApJL*, 768, 172
 Conroy, C., Graves, G. J., & van Dokkum, P. G. 2014, *ApJL*, 780, 33
 Conroy, C., & van Dokkum, P. 2012a, *ApJL*, 747, 69
 Conroy, C., & van Dokkum, P. G. 2012b, *ApJL*, 760, 71
 Conroy, C., van Dokkum, P. G., & Villaume, A. 2017, *ApJL*, 837, 166
 Conroy, C., Villaume, A., van Dokkum, P. G., & Lind, K. 2018, *ApJ*, 854, 139
 Dalcanton, J. J., Spergel, D. N., Gunn, J. E., Schmidt, M., & Schneider, D. P. 1997, *AJ*, 114, 635
 Drory, N., MacDonald, N., Bershady, M. A., et al. 2015, *AJ*, 149, 77
 Foreman-Mackey, D. 2016, corner.py: corner.py v2.0.0, Zenodo, doi:10.5281/zenodo.53155
 Foreman-Mackey, D., Hogg, D. W., Lang, D., & Goodman, J. 2013, *PASP*, 125, 306
 Gallazzi, A., Charlot, S., Brinchmann, J., & White, S. D. M. 2006, *MNRAS*, 370, 1106
 Gallazzi, A., Charlot, S., Brinchmann, J., White, S. D. M., & Tremonti, C. A. 2005, *MNRAS*, 362, 41
 Geller, M. J., Diaferio, A., & Kurtz, M. J. 1999, *ApJL*, 517, L23
 Graves, G. J., Faber, S. M., & Schiavon, R. P. 2009, *ApJL*, 693, 486
 Gunn, J. E., Siegmund, W. A., Mannery, E. J., et al. 2006, *AJ*, 131, 2332
 Impey, C., Bothun, G., & Malin, D. 1988, *ApJL*, 330, 634
 Kadowaki, J., Zaritsky, D., & Donnerstein, R. L. 2017, *ApJL*, 838, L21
 Kirby, E. N., Cohen, J. G., Guhathakurta, P., et al. 2013, *ApJ*, 779, 102
 Koda, J., Yagi, M., Yamanoi, H., & Komiyama, Y. 2015, *ApJL*, 807, L2
 Kroupa, P. 2001, *MNRAS*, 322, 231
 Kurucz, R. L. 1970, SAOSR, 309
 Kurucz, R. L. 1993, Kurucz CD-ROM (Cambridge, MA: Smithsonian Astrophysical Observatory)
 Law, D. R., Cherinka, B., Yan, R., et al. 2016, *AJ*, 152, 83
 Law, D. R., Yan, R., Bershady, M. A., et al. 2015, *AJ*, 150, 19
 Leisman, L., Haynes, M. P., Janowiecki, S., et al. 2017, *ApJL*, 842, 133
 Liu, M. C., & Graham, J. R. 2001, *ApJL*, 557, L31
 Liu, Y., Peng, E. W., Blakeslee, J., et al. 2016, *ApJL*, 818, 179
 Lu, Y., Benson, A., Wetzel, A., et al. 2017, *ApJ*, 846, 66
 Ma, X., Hopkins, P. F., Kasen, D., et al. 2016, *MNRAS*, 459, 3614
 Martínez-Delgado, D., Läsker, R., Sharina, M., et al. 2016, *AJ*, 151, 96
 Merritt, A., van Dokkum, P., Danieli, S., et al. 2016, *ApJL*, 833, 168
 Mihos, J. C., Durrell, P. R., Ferrarese, L., et al. 2015, *ApJL*, 809, L21
 Mobasher, B., Bridges, T. J., Carter, D., et al. 2001, *ApJS*, 137, 279
 Muñoz, R. P., Eigenthaler, P., Puzia, T. H., et al. 2015, *ApJL*, 813, L15
 Peng, E. W., & Lim, S. 2016, *ApJL*, 822, L31
 Penny, S. J., & Conselice, C. J. 2008, *MNRAS*, 383, 247
 Rines, K., Geller, M. J., Diaferio, A., & Kurtz, M. J. 2013, *ApJL*, 767, 15
 Román, J., & Trujillo, I. 2017, *MNRAS*, 468, 703
 Rong, Y., Guo, Q., Gao, L., et al. 2017, *MNRAS*, 470, 4231
 Sánchez-Blázquez, P., Peletier, R. F., Jiménez-Vicente, J., et al. 2006, *MNRAS*, 371, 703
 Sandage, A., & Binggeli, B. 1984, *AJ*, 89, 919
 Schlafly, E. F., & Finkbeiner, D. P. 2011, *ApJL*, 737, 103
 Smee, S. A., Gunn, J. E., Uomoto, A., et al. 2013, *AJ*, 146, 32
 Smith, R. J., Lucey, J. R., Hudson, M. J., et al. 2009, *MNRAS*, 392, 1265
 Sohn, J., Geller, M. J., Zahid, H. J., et al. 2016, *ApJS*, 229, 20
 Thomas, D., Maraston, C., Schawinski, K., Sarzi, M., & Silk, J. 2010, *MNRAS*, 404, 1775
 Trager, S. C., Faber, S. M., & Dressler, A. 2008, *MNRAS*, 386, 715
 Trager, S. C., Faber, S. M., Worthey, G., & González, J. J. 2000, *AJ*, 119, 1645
 van der Burg, R. F. J., Muzzin, A., & Hoekstra, H. 2016, *A&A*, 590, A20
 van Dokkum, P., Abraham, R., Brodie, J., et al. 2016, *ApJL*, 828, L6
 van Dokkum, P., Abraham, R., Romanowsky, A. J., et al. 2017, *ApJL*, 844, L11
 van Dokkum, P. G., Abraham, R., & Merritt, A. 2014, *ApJL*, 782, L24
 van Dokkum, P. G., Abraham, R., Merritt, A., et al. 2015a, *ApJL*, 798, L45
 van Dokkum, P. G., Romanowsky, A. J., Abraham, R., et al. 2015b, *ApJL*, 804, L26
 van Zee, L., Barton, E. J., & Skillman, E. D. 2004, *AJ*, 128, 2797
 Villaume, A., Conroy, C., Johnson, B., et al. 2017, *ApJS*, 230, 23
 Wolf, J., Martínez, G. D., Bullock, J. S., et al. 2010, *MNRAS*, 406, 1220
 Worthey, G. 1994, *ApJS*, 95, 107
 Yagi, M., Koda, J., Komiyama, Y., & Yamanoi, H. 2016, *ApJS*, 225, 11
 Yan, R., Bundy, K., Law, D. R., et al. 2016a, *AJ*, 152, 197
 Yan, R., Tremonti, C., Bershady, M. A., et al. 2016b, *AJ*, 151, 8
 Zahid, H. J., Kudritzki, R.-P., Conroy, C., Andrews, B., & Ho, I.-T. 2017, *ApJ*, 847, 18